Predicting Low-Level Wind Shear Using 200-m-Resolution NWP at the Hong Kong International Airport

KAI-KWONG HON

Hong Kong Observatory, Hong Kong, China

(Manuscript received 1 August 2019, in final form 6 December 2019)

ABSTRACT

"Low-level wind shear" is a known aviation safety hazard and refers to a sustained change in head wind encountered by an aircraft during takeoff or landing. Because of their small spatiotemporal scales and high variability, automatic alerting of wind shears at airports around the world is almost exclusively detection based (using remote sensing equipment). Numerical modeling studies so far mainly cover individual cases and lack systematic validation. This paper presents the first statistical evaluation of numerical weather prediction (NWP) model performance in predicting low-level wind shear at a major international airport over a 2-yr continuous period. The 200-m-resolution Aviation Model (AVM) of the Hong Kong Observatory is used to generate runway-specific wind shear forecasts at 1-min output intervals for the Hong Kong International Airport (HKIA), known for its susceptibility to wind shear occurrence. The AVM forecasts are then validated against over 800 actual reports of wind shear by aircraft pilots over the two major arrival runway corridors, 07LA and 25RA, at HKIA between 2014 and 2015 using a verification scheme with the same level of spatiotemporal stringency as operational alerting systems at HKIA. With "relative operating characteristic" analysis, positive skill is consistently observed across both runway corridors throughout the study period and across all considered forecast lead times out to 6 h ahead. This study serves to establish and document the current capability of fine-resolution NWP in predicting the phenomenon of low-level wind shear for aviation weather applications.

1. Introduction

Low-level wind shear, defined as a sustained head wind (i.e., winds blowing in the opposite direction to aircraft motion) change of 15 kt (~7.7 m s^{-1}) or more at an altitude of 1600 ft (~488 m) or below, is a known aviation safety hazard (ICAO 2005, 2007). In aviation meteorology, there are in fact a number of phenomena related to spatial and/or temporal variations in the three-dimensional wind fields that are of safety interest or concern. For example, an aircraft during the level phase of flight at cruising levels (normally ranging from 30 000 to 40 000 ft above sea level; 1000 ft ≈ 0.3 km) may be susceptible to clear-air turbulence (CAT), which is linked to shear and deformation under suitable stability conditions (Ellrod and Knapp 1992; Ellrod and Knox 2010). Within the boundary layer (typically the lowest 1 or 2 km of the troposphere) there is also emphasis on the vertical shear of the horizontal winds (ICAO 2005). In this paper, we focus on the variation, or shear, of the horizontal wind component along the aircraft trajectory, specifically during the takeoff and landing phases of flight (termed "low-level wind shear" or "wind shear" in subsequent paragraphs; Hong Kong Observatory 2010). Such wind shear is important from a safety point of view because it is the head wind that provides aerodynamical lift for an aircraft in motion. Rapid or large changes in head wind can bring about significant changes in lift and hence altitude of the aircraft. During the takeoff and landing phases of flight, the aircraft normally have relatively low airspeeds (e.g., when compared with the speed at cruising levels) but are in close proximity to the ground. This means that there is little room for corrective measures that are based on the speed–altitude tradeoff (Proctor et al. 2000) that is effective at higher altitudes.

Wind shear may be caused by a variety of mesoscale or microscale meteorological phenomena with different physical mechanisms and flow regimes, including

Denotes content that is immediately available upon publication as open access.

Corresponding author: Kai-Kwong Hon, kkhon@hko.gov.hk

DOI: 10.1175/JAMC-D-19-0186.1

thunderstorm downburst (or, in its most severe form, known as microburst to the aviation community), which possesses characteristics of a density current (Hall et al. 1976; Fujita 1978), terrain-disrupted airflow with or without a temperature inversion (Chan and Hon 2016a,b), frontal passage, tropical cyclones, land/sea-breeze circulation, and so on (Lau 2000; Chan et al. 2010), all of which are capable of inducing significant gradients in the horizontal wind components. These wind shear–inducing meteorological phenomena may occur with or without precipitation.

The availability of dedicated, high-resolution remote sensing instruments such as the Terminal Doppler Weather Radar (TDWR, which works effectively in rain) (Wilson and Wakimoto 2001) and the Doppler light detection and ranging (lidar, which works effectively in clear-air conditions) (Shun and Chan 2008) have greatly benefitted the understanding and hence detection of low-level wind shear at airports around the world. There are various successful, operational examples of automatic low-level wind shear alerting systems based on remote sensing and/or in situ measurement equipment (Shun 2004; Matayoshi et al. 2016; Robinson et al. 2017). So far, these methods are detection or observation based (i.e., issuing an alert when the phenomenon is observed) and do not involve predicting future occurrences of the phenomena through objective application of known physical laws.

There have also been literature attempts at prediction or simulation of wind shear conditions using different forms of numerical modeling techniques, including computer fluid dynamics (Li et al. 2013), large-eddy simulations (LES) (Cheung et al. 2011), numerical weather prediction (NWP) (Clark et al. 1997; Chan and Hon 2016a), and shallow-water models (Carruthers et al. 2014). These studies were generally performed on a case-study basis and covered single or isolated episodes of reported wind shear events. There is a lack of long-term, systematic evaluation of the predictive capability of numerical models in capturing low-level wind shear occurrences.

In this paper, we investigate the performance of the Aviation Model (AVM), which is the subkilometer-resolution NWP suite operated by the Hong Kong Observatory (HKO), in short-term forecasts of low-level wind shear at the Hong Kong International Airport (HKIA) over a 2-yr period. The HKIA is constructed on an artificial island surrounded by open waters on three sides but in close proximity to the mountainous Lantau Island (with an elevation up to over 900 m above sea level) to its south. The complex orography and intricate land–sea contrast are favorable ingredients for the occurrence of low-level wind shear at HKIA, which is well documented by many observational and modeling studies (Shun and Lau 2000; Szeto and Chan 2006; Tang et al. 2011a,b). This study presents the first long-term verification results in low-level wind shear prediction using an operational NWP model. The spatial resolution of the model in continuous operational use (200 m) and the coverage of the study period (2 yr) make this study a unique contribution to the literature.

This paper is organized as follows. Section 2 gives the technical description of the AVM. Section 3 describes the method for generating wind shear forecasts from the AVM and the verification method including observational data. Selected cases of wind shear features as successfully predicted by the AVM are presented in section 4. Section 5 presents and discusses long-term verification results of the AVM wind shear forecasts. Conclusions are given in section 6.

2. Model description

AVM (Chan and Hon 2016b; Hon 2018) is a subkilometer-resolution implementation of the Weather Research and Forecasting (WRF) (Skamarock and Klemp 2008) Model by the HKO for finescale short-term weather prediction at HKIA. During the course of this study (spanning 2014–15), version 3.4.1 of the WRF Model was in use. The AVM comprised two singly nested domains (Fig. 1): AVM-PRD (''PRD'' refers to the Pearl River Delta to the west of Hong Kong) at 600-m horizontal resolution and AVM-HKA (''HKA'' refers to HKIA) at 200-m horizontal resolution. The AVM-PRD domain is about 350 km × 350 km in dimension (with 581 × 581 horizontal grid points) and covers the whole territory of Hong Kong, China, and its immediate vicinity. The AVM-HKA domain is about 50 km × 50 km in dimension (with 253 × 253 horizontal grid points) and is centered around HKIA. As a compromise between vertical resolution and constraints in computational resources, 42 eta levels were used, of which at least 10 were below 1000 m at the time of model initialization. It is acknowledged that such a vertical resolution would be far from ideal—experiments on subkilometric NWP in other parts of the world (some including aviation applications but not specific to the problem of low-level wind shear) have been reported to utilize between 70 vertical layers [e.g., the ''London Model'' at 333-m resolution in Boutle et al. (2016)] to over 100 vertical layers [e.g., the ''AROME Airport'' at 500-m resolution in Hagelin et al. (2014); the Icosahedral Nonhydrostatic Atmosphere (ICON) model at 156-m resolution in Heinze et al. (2017)]. However, note that some of the above examples are run on a one-off basis (i.e., without the operational demand to meet a real-time forecast schedule), whereas for one of the real-time

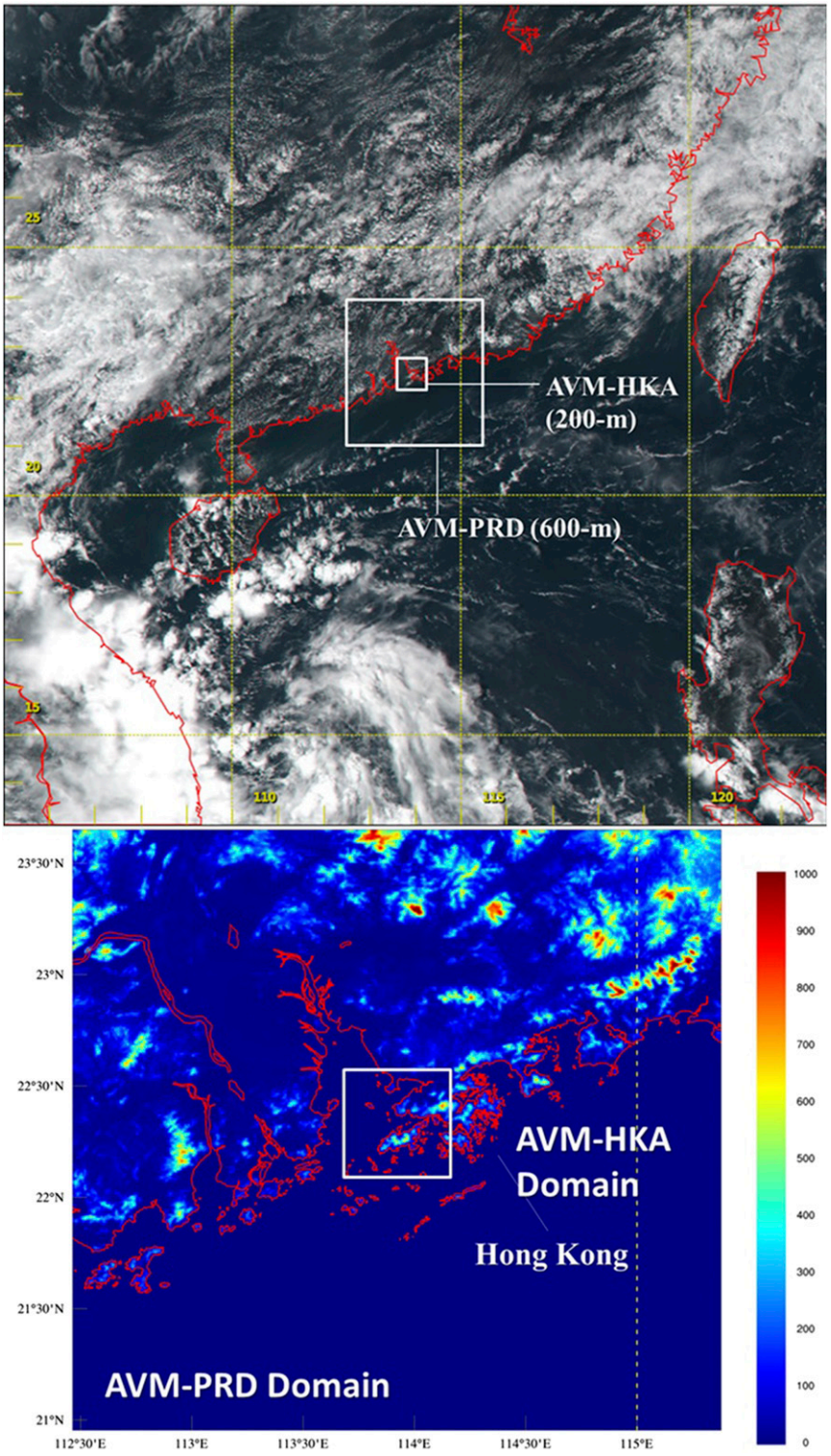

FIG. 1. The forecast domains of the 600-m-resolution AVM-PRD and 200-m-resolution AVM-HKA. (top) The two domains, with background satellite imagery of the visible channel of the *Himawari-8*, provided through the courtesy of the Japan Meteorological Agency.

examples the authors through testing found little difference in further refinement of vertical resolution. The latter is similar to the experience at HKO during the early testing stages of AVM and also studies in other parts of the world (Zhang et al. 2013). As will be seen from the sample cases in section 4 below, the existing configuration of AVM, although not ideal, is generally considered to be usable and acceptable for various weather conditions typically experienced at HKIA, as based on day-to-day inspection by experienced aviation weather forecasters.

The AVM is run every hour to provide 6–9-h short-term forecasts for HKIA. Initial and boundary conditions of AVM-PRD are provided by the latest available forecast (usually initialized 1–2 h earlier) of the "RAPIDS-NHM" (Wong 2010; NHM indicates a nonhydrostatic model), which is HKO's operational mesoscale model at 2-km resolution. Initial and boundary conditions of AVM-HKA are in turn provided by the concurrent AVM-PRD forecast through 1-way nesting. For both AVM-PRD and AVM-HKA, 3D variational data assimilation based on the WRF Data Assimilation System (WRFDA) is used to ingest conventional surface and upper-air observations as well as the dense network of surface observations over the inland Guangdong Province. The normal data cutoff time is 15 min past every hour (e.g., for the 0000 UTC model run, we wait until 0015 UTC to collect all available observations valid at 0000 UTC before performing data assimilation). To adhere to the hourly schedule, each model run (including preprocessing, data assimilation, model integration, and postprocessing routines) is completed within 60 min and is normally available to the aviation weather forecasters at HKIA around 15 min past the subsequent hour (e.g., output from the 0000 UTC model run is viewable/usable around 0115 UTC).

Model settings of the AVM follow that of Chan and Hon (2016b). Key configurations include the WRF double-moment six-class microphysics (WDM6) scheme (Lim and Hong 2010), RRTMG schemes for short- and longwave radiation (Iacono et al. 2008), and the Noah land surface model (Niu et al. 2011). Given the high horizontal resolution, no cumulus parameterization is used. AVM-PRD uses the MYJ boundary layer parameterization (Mellor and Yamada 1982; Janjić 2001) whereas AVM-HKA is run without a boundary layer scheme (i.e., using the "LES" mode). In place of the boundary layer scheme, vertical diffusion is handled by the Smagorinsky approach with the diffusivity diagnosed from the deformation term. The default value of the constant Smagorinsky coefficient in the WRF Model (i.e., $C_s = 0.18$) is used. It is understood that there are inherent limitations in this formulation, particularly when near a "wall" (e.g., Talbot et al. 2012), which in the case of AVM-HKA means being adjacent to the presence of model terrain. Both domains utilize the U.S. Geological Survey 3-s topography and MODIS land-use data, with local adaptations to cater to urbanization and changes in coastline. To provide additional savings in computational time during model integration, adaptive time stepping was used for both domains of the AVM. For the 200-m-resolution AVM-HKA, under the prescribed Courant number limit of 1.05, an integration time step between 3 and 5 s can be achieved under most weather conditions, but a smaller step (occasionally down to 1–2 s) is needed during organized convection or on particularly windy days.

3. Method and observation data

In this paper, we use forecast output from the 200-m-resolution AVM-HKA domain. The capability of the AVM-HKA in capturing the spatiotemporal behavior of finescale wind features around HKIA has been reported in a number of papers (Chan and Hon 2016a,b). Following Hon and Chan (2017), forecast head wind profiles are generated at 1-min output frequency to emulate the specialized lidar scans in use for operational wind shear detection at HKIA (Shun and Chan 2008). These head wind profiles are computed by extracting the horizontal wind vector on the closest grid points along the three-dimensional aircraft glide path during takeoff and landing at HKIA, then decomposing along the runway direction (heading angle of 70° or 250°) to obtain the head wind component. The glide paths are assumed to extend along the runway direction at an elevation angle of 3° for landing or 6° for takeoff flights. To approximate the geometry of the aircraft glide path, wind vectors extracted from the nearest model levels are interpolated vertically (but not horizontally, to preserve spatial variability) assuming logarithmic linearity in height. The resultant forecast head wind profile is a spatial series of the head wind component of the horizontal wind vectors interpolated onto the three-dimensional, slanted aircraft glide path for each runway corridor at HKIA. This is a prediction of the head wind as would be experienced by an aircraft landing or taking off along that particular flight path. Conventionally, positive head wind is taken as winds blowing against the direction of flight. Negative head wind (or tailwind) is taken as winds blowing along the direction of flight. Since there are two runways at HKIA (the north runway and the south runway), and each runway can in principle be used for takeoff or landing at either ends (heading angle of 70° or 250°), there are a maximum of eight possible configurations (or runway corridors). AVM-HKA produces

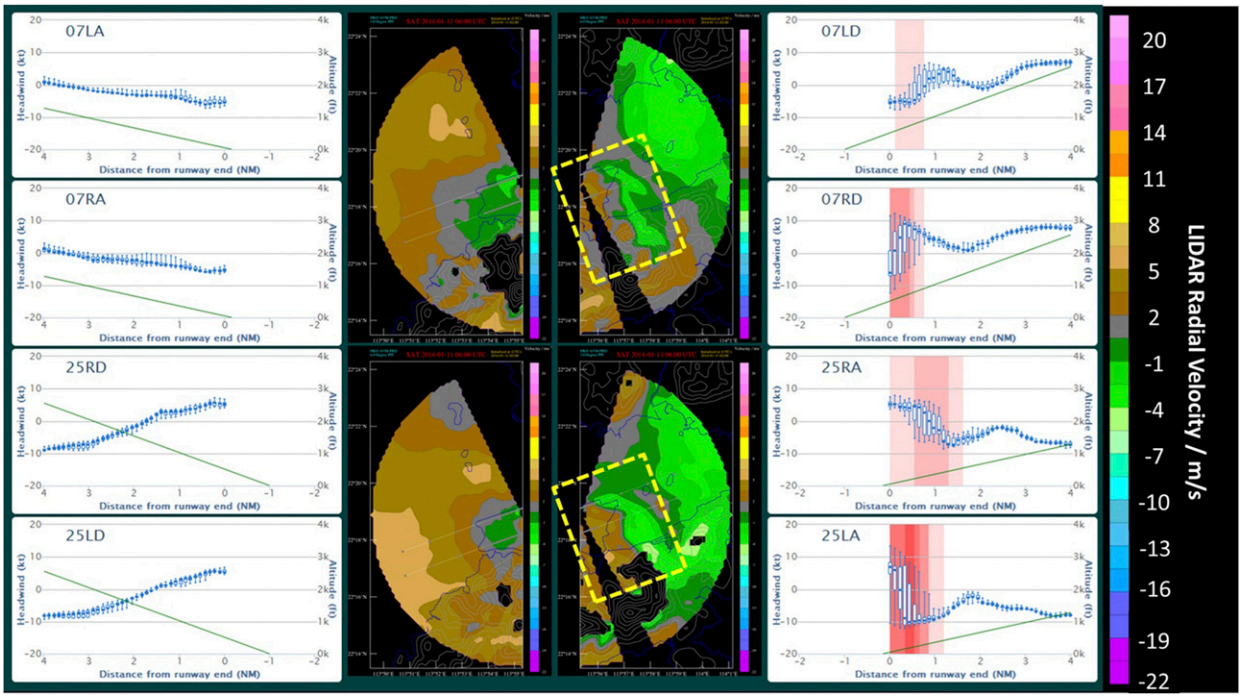

FIG. 2. Display panel of wind shear forecasts by AVM-HKA for 11 Jan 2014 in the form of simulated Doppler lidar return (the color scale is given on the right). This is a 4-h forecast by AVM-HKA valid at 0600 UTC and initialized at 0200 UTC. (left),(right) Box-and-whisker plots combining sixty 1-min forecast head wind profiles between 0600 and 0659 UTC for each of the eight runway corridors of HKIA. (center) The simulated planar scans at elevation angles of 3° and 6°. The converging winds resulting from a sea-breeze front are highlighted by the dashed yellow-outlined rectangles. During this hour, there are four PIREPs at runway corridor 07RD.

forecast head wind profiles for all eight runway corridors (Fig. 2) out to a distance of 4 n mi (1 n mi = 1.852 km) from the respective runway endpoints. In practice, the north runway is the predominant landing runway at HKIA. Landing on the north runway from the western side (i.e., heading angle of 70°) is known as using runway corridor "07LA" while landing on the north runway from the eastern side is known as using runway corridor "25RA."

To generate a binary prediction of wind shear ("yes" or "no") at a particular time, it is necessary to identify from the forecast head wind profile of AVM-HKA the existence of any sustained head wind changes occurring within a certain distance. One possible choice is to directly apply the "ramp identification algorithm" of HKO's lidar wind shear alerting system (Jones and Haynes 1984) to the forecast head wind profiles. Here we adopt an alternative approach loosely based on the concept of head wind gradient similar to Chan et al. (2011). Given a head wind profile $H_i(x)$, where H is the head wind (in knots) along the ith runway corridor at a distance of x nautical miles from the runway endpoint, the maximum and minimum head wind within a specified window, $H_{\max,L}$ and $H_{\min,L}$, where L is the distance of the specified window in nautical miles, are first identified. The pair of $H_{\max,L}$ and $H_{\min,L}$ that maximizes the value of their absolute difference (i.e., producing the largest head wind change) is then picked out. The absolute difference of this pair will be labeled ΔH_L, the maximum head wind change under a given L, for this particular head wind profile. In this way, a binary prediction of wind shear can be generated from a head wind profile by applying a threshold to ΔH_L. It is necessary to constrain the maximum length over which the head wind changes occur because gentle gradients (i.e., changes spreading out over a long distance) are often not regarded by aircraft pilots as wind shear events (Hong Kong Observatory 2010).

This study covers the 2-yr period from January 2014 to December 2015. Hourly forecasts by AVM-HKA will be validated against reports of wind shear occurrence by pilots landing at or taking off from HKIA [pilot reports (PIREPs)]. As an established practice at HKIA, pilots of landing and departing aircraft may provide reports of low-level wind shear (and turbulence, which is considered to be a separate phenomenon in terms of reporting and alerting at HKIA) encounters to air traffic control either directly through onboard radio communication or by submitting a report form afterward. This is different from conventional PIREPs of turbulence and icing,

which normally cover the en-route phase of flight. The HKIA wind shear PIREPs contain information on the timing, location (normally reported to the nearest nautical mile), altitude (normally reported to the nearest 50 or 100 ft), and perceived intensity [normally reported to the nearest 5 kt (1 kt $\approx$ 0.51 m s^{-1}), e.g., −25 kt, with positive or negative signs representing gain or loss in head wind, respectively] of an event. All received PIREPs underwent basic quality control to flag those reported events that fall outside the scope of HKO's low-level wind shear alerting service, namely 1) the reported absolute magnitude must be 15 kt or greater and 2) the location of occurrence must be below 1600 ft (used interchangeably with 500 m) or within 3 n mi from touchdown/takeoff. Since the majority of PIREPs are received over 07LA and 25RA, we will focus only on these two runway corridors in the following paragraphs. Out of the 584 PIREPs received in 2014, 268 (45.9%) occurred over 07LA and 129 (22.1%) were over 25RA. For 2015, of the 558 PIREPs received, 293 (52.5%) occurred over 07LA and 148 (26.5%) were over 25RA.

Verification is performed using the ''relative operating characteristics'' (ROC) diagram (Wilks 2006), which has been employed in different studies on wind shear detection in the past (Chan et al. 2011; Lee and Chan 2014). A threshold-based approach is applied such that an alert is triggered for a runway corridor whenever the value of ΔH_L from a forecast head wind profile for that particular runway corridor exceeds a predetermined threshold. If a PIREP at the same runway corridor occurs within 4 min after an alert is triggered, a ''hit'' is recorded. This is identical to the verification scheme in use for actual alerts of low-level wind shear (i.e., those issued automatically using lidar detection) at HKIA by HKO. Following Wu and Hon (2018), the percentage of detection (PoD) and percentage of time on alert (PoTA), which form respectively the vertical and horizontal axes of the resultant ROC diagram, are defined as

$$\text{PoD} = \frac{\text{No. of hits}}{\text{Total no. of pilot reports}} \times 100\% \quad \text{and}$$

$$\text{PoTA} = \frac{\text{Alert duration}}{\text{Total length of time investigated}} \times 100\%,$$

where the ''alert duration'' is the length of time (in minutes) for which an alert from the AVM forecast is issued and the ''total length of time investigated'' is the length of the study period (also in minutes). This modified formulation of the ROC diagram has been in use (since well before the study period of this paper) for verification of HKO's low-level wind shear alerts with aviation users' acceptance, and it is also reported in a number of other papers (Hon and Chan 2014a,b).

4. Selected cases of wind shear features forecast by AVM-HKA

It might be illustrative to present a few cases of AVM-HKA forecasts that correspond to actual, reported occurrence of wind shear at HKIA. The three cases described below all occurred under different weather conditions.

The first case is related to sea breeze. On 11 January 2014, the prevailing winds at HKIA were light under weak synoptic forcing. Sea breeze caused by differential heating of the HKIA island and its surrounding waters set in during the early afternoon. Figure 2 shows the wind shear forecast display panel for this case, as made available to aviation weather forecasters of HKO in real time. This is a 4-h forecast valid at 0600 UTC, initialized at 0200 UTC the same day. As described in Chan and Hon (2016b), the middle columns show the simulated Doppler velocity distribution around HKIA assuming fixed elevation scans at 3° and 6° by an imaginary Doppler lidar located at the center of the circle. The legend for interpreting the color contours of the simulated Doppler velocity distributions is shown on the right of Fig. 2. In this color scale, ''warm'' colors (e.g., pink, yellow, and brown) are used to represent different strengths of flows away from the lidar (positive Doppler velocities). Similarly, ''cool'' colors (e.g., green, blue, and magenta) are used to represent different strengths of flows into the lidar (negative Doppler velocities). The highlighted area shows alternating brown and green colors on the eastern side of HKIA. Since this area of brown and green colors occur to the east of the (imaginary) lidar, the brown colors within the highlighted region would translate to winds blowing away from the lidar toward the east (i.e., westerly winds). Similarly, the green colors within the highlighted region would translate to winds blowing toward the lidar from the east (i.e., easterly winds). This corresponds to the opposing, or converging, winds resulting from a sea-breeze front at that position and is a typical signature for lidar observations of sea-breeze features. The box-and-whisker plots on the left and right columns of Fig. 2 also follow the presentation in Chan and Hon (2016b). There is one plot for each runway corridor of HKIA. Each plot is the resultant of 60 forecast head wind profiles, at 1-min output interval, for that runway corridor during that forecast hour (0600–0659 UTC). The highlighted regions show potential occurrence of wind shear as seen from the sustained changes in head wind, ranging from −10 to +10 kt. Since the sea-breeze front is

forecast to occur at the eastern side of HKIA, only the runway corridors on the right show possible wind shear features. During this hour, four PIREPs were received over 07RD, where possible occurrence of wind shear had been forecast. (Note that at HKIA only one arrival and one departure runway corridor could be simultaneously in use.) The corresponding temporal evolution of AVM-HKA forecast head wind profiles over 07RD during this case is illustrated in Fig. 3.

The second case is related to thunderstorm downbursts. The capability of the AVM to capture complex wind features associated with convection is recently reported in Hon et al. (2019). On 4 September 2014, isolated thunderstorms affected the western parts of Hong Kong in the afternoon. Figures 4a and 4b show the forecast radar reflectivity by AVM-HKA and actual radar observations at 0600 UTC. The thunderstorms occurred around 10 km northeast of HKIA and did not directly affect the airport. However, thunderstorm outflow or downbursts spread southwestward to affect the eastern runway corridors of HKIA such that around 0600 UTC there was one PIREP at 25RA. It can be seen from Fig. 4c that the 6-h forecast from AVM-HKA (initialized at 0000 UTC of the same day) successfully captured the wind shear feature due to convergence between prevailing north or northwesterly winds and thunderstorm-induced easterly winds to the east of HKIA. The corresponding temporal evolution of AVM-HKA forecast head wind profiles over 25RA during this case is illustrated in Fig. 5.

The third case is related to terrain-disrupted airflow, which is relatively well documented for the AVM (Chan et al. 2020). On 28 February 2015, Hong Kong was under the influence of a late-season northeast monsoon, with surface winds mainly blow from the east that then gradually veered to southeasterly with height. This wind regime is known to be conducive to occurrence of significant wind shear at HKIA (Leung et al. 2018). In Fig. 6, it can be seen that significant mountain wake flow occurred at the western side of HKIA downstream of the Lantau mountains. In particular, the forecast head wind profiles for the western runway corridors all depicted sharp head wind changes ranging from −10 to +15 kt at different positions. Here the AVM-HKA forecast is valid at 0200 UTC and initialized at 2100 UTC of the previous day. During this hour, there were 10 PIREPs over 07LA. For this prolonged wind shear episode, the temporal evolution of AVM-HKA forecast head wind profiles over 07LA is illustrated in Fig. 7.

The above examples show that short-term forecasts by the 200-m-resolution AVM-HKA are capable of predicting correctly, under a number of different weather conditions, low-level wind shear features that are reported to be significant by pilots landing at or taking off from HKIA.

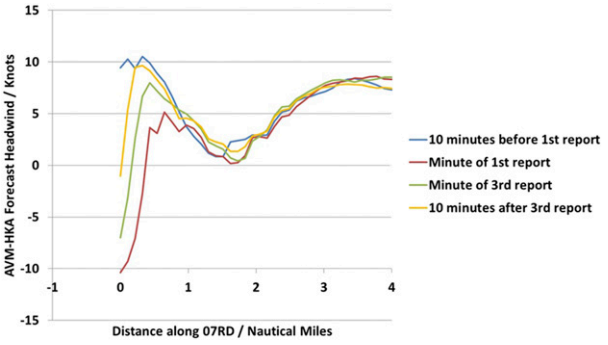

FIG. 3. Evolution of AVM-HKA forecast head wind profile during the sea-breeze-induced wind shear event over runway corridor 07RD as illustrated in Fig. 2. Here the aircraft takes off toward the right-hand side (from the 0 n mi position eastward toward the 4 n mi position). The same AVM-HKA run as in Fig. 2 is used. The head wind profiles shown here cover three of the four PIREPs mentioned in Fig. 2. These three PIREPs occurred successively within a 5-min window. Evolution of the wind shear feature as a result of sea-breeze onset is as follows: 10 min before the first report (blue line) the head wind variations at 07RD are relatively gentle, between 0 and 10 kt only; by the time of the first PIREP (red line), a sharp head wind change is observed between 0 and 1 n mi (changing from −10 to +5 kt; i.e., wind shear of ~15 kt) where the sea-breeze front occurred; this feature sustained in intensity until the third PIREP (green line); thereafter it weakened (yellow line; valid at 10 min after the third PIREP) such that the extent of head wind change decreased to only ~10 kt (changing from 0 to +10 kt) while remaining at the same location (between 0 and 1 n mi).

5. Verification results and discussion

As described in section 3, verification of the wind shear forecasts by AVM-HKA will utilize the ROC diagram. Figures 8 and 9 are the ROC diagrams for runway corridor 07LA over 2014 and 2015, respectively. Figures 10 and 11 are the same diagrams for runway corridor 25RA. Forecasts up to 6 h ahead are used in the verification. These are represented by different colors in the diagrams as explained in the legends. Since the forecast head wind profiles by AVM-HKA are generated in 1-min output intervals, and PIREPs are also timestamped to the minute, in these diagrams a "$T + 0$" forecast by AVM-HKA refers to a forecast head wind profile with valid time between $T + 0$ and $T + 59$ min (i.e., the zeroth hour), a "$T + 1$" forecast refers to between $T + 1$ h and $T + 1$ h 59 min, and so on (Unfortunately "$T + 0$" forecast data, marked by black dotes, had not been archived for 2015 and are therefore not available.) For each forecast lead time, a family of ROC curves is generated following the manner of Wu and Hon (2018) by applying a range of thresholds to

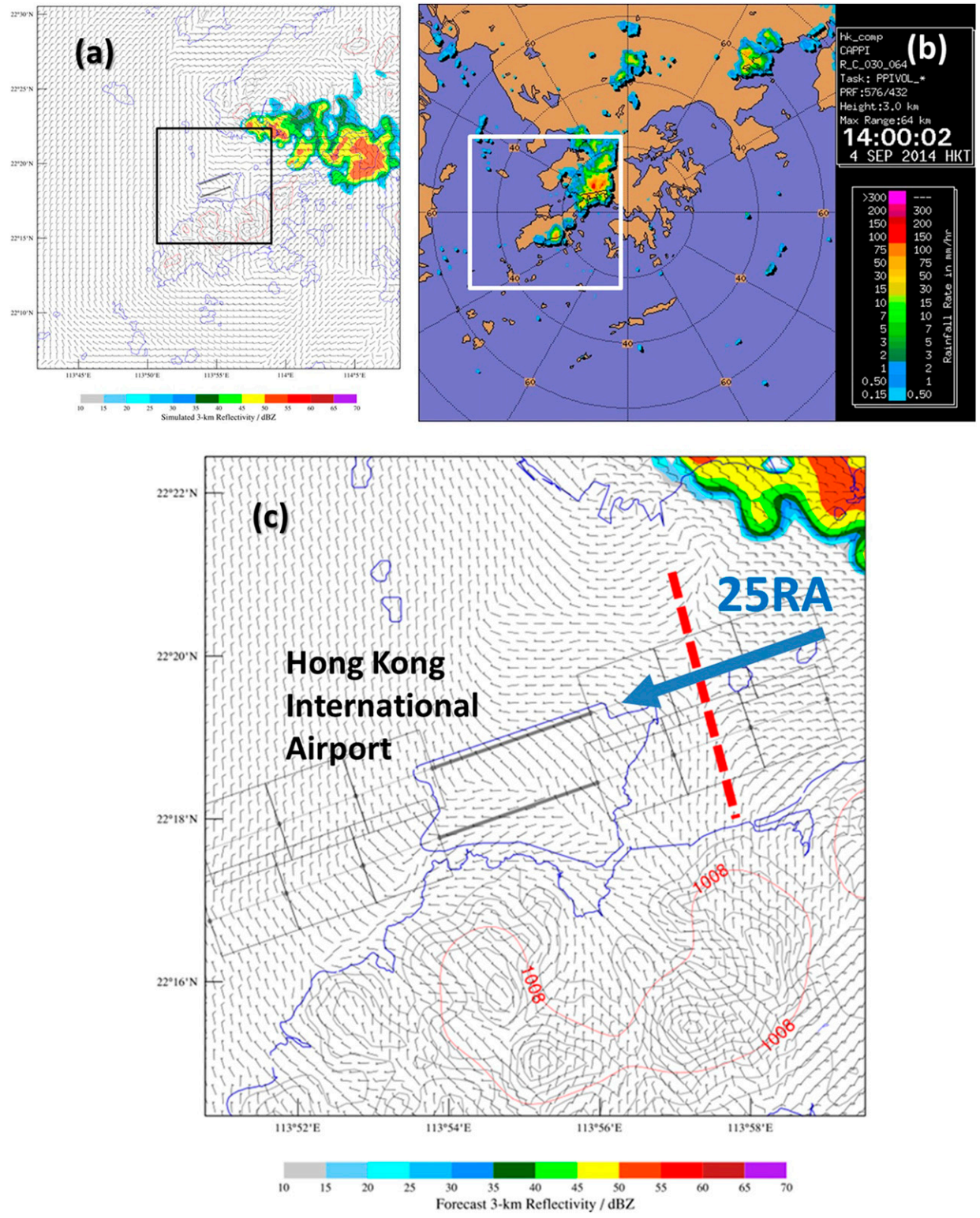

FIG. 4. Isolated thunderstorms as (a) simulated by AVM-HKA and (b) observed by weather radar on the afternoon of 4 Sep 2014. This is a 6-h forecast valid at 0600 UTC and initialized at 0000 UTC. The coverage of (a) is given by the white-outlined square in (b). The area of the zoom-in plot of (c) is shown by the black-outlined square marked in (a). It can be seen in (c) that the thunderstorm outflow in the form of easterly winds of 10–15 kt has spread to the east of HKIA. The line of wind shear–inducing convergence is marked in red. During this hour, there is one PIREP over runway corridor 25RA that is landing from the east using the north runway of HKIA.

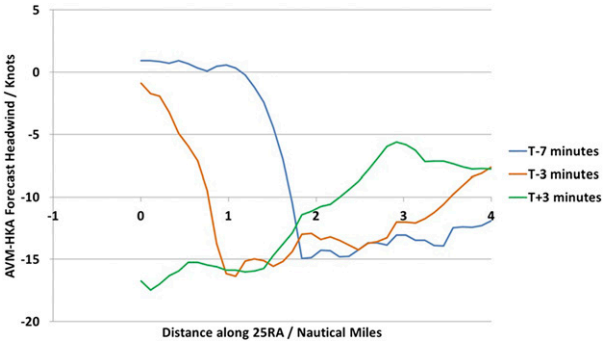

FIG. 5. Evolution of AVM-HKA forecast head wind profile during the thunderstorm-induced wind shear event over runway corridor 25RA as illustrated in Fig. 4. Here the aircraft lands from the right-hand side (from the 4 n mi position to the 0 n mi position, which is touchdown). The same AVM-HKA run as in Fig. 4 is used. The propagation of the wind shear feature is evident from the line plots taken at different times around the event: the sharp head wind change (blue line, valid at 7 min before the event) occurring between 1 and 2 n mi gradually shifted westward to between 0 and 1 n mi (orange line; valid at 3 min before the event) and finally departed from the runway corridor (green line; valid at 3 min after the event).

the parameters ΔH_L and L, which have been defined in section 3. The ranges of ΔH_L and L considered are respectively head wind differences of 0.5–15 kt and length scales of 0.5–2 n mi, which are similar to those used in observation-based studies involving lidars. This leads to a collection of points in the two-dimensional (PoD, PoTA) space that are then plotted onto the ROC diagrams. If these points (which collectively we refer to as the "curve" or "family of curves") lie along the diagonal, there is no skill in the detection method in differentiating between events and nonevents. Proximity to the top-left corner indicates increasing skill level.

It is immediately obvious that the AVM-HKA forecasts exhibit positive skill over both 07LA and 25RA consistently across the 2-yr study period and throughout the available forecast hours out to $T + 6$. Although there are some subtle differences in the shape of the individual ROC curves (such as the location or curvature of the "shoulder"), all curves are away from the diagonal and convex toward the top-left (i.e., skillful) corner of the diagrams. Note that the rightmost points in the ROC curves may not reach the top-right corner because of model downtime resulting from system maintenance.

Assuming a characteristic PoTA of 20%, the PoD for 07LA would range between 40% and 60%. The values are similar for 25RA. Since this is the first time that NWP forecasts of wind shear have been systematically validated, there is no readily available "benchmark" for direct comparison. However, under the context of aviation weather hazards, we may draw a loose analogy with the prediction of upper-air CAT by convection-permitting

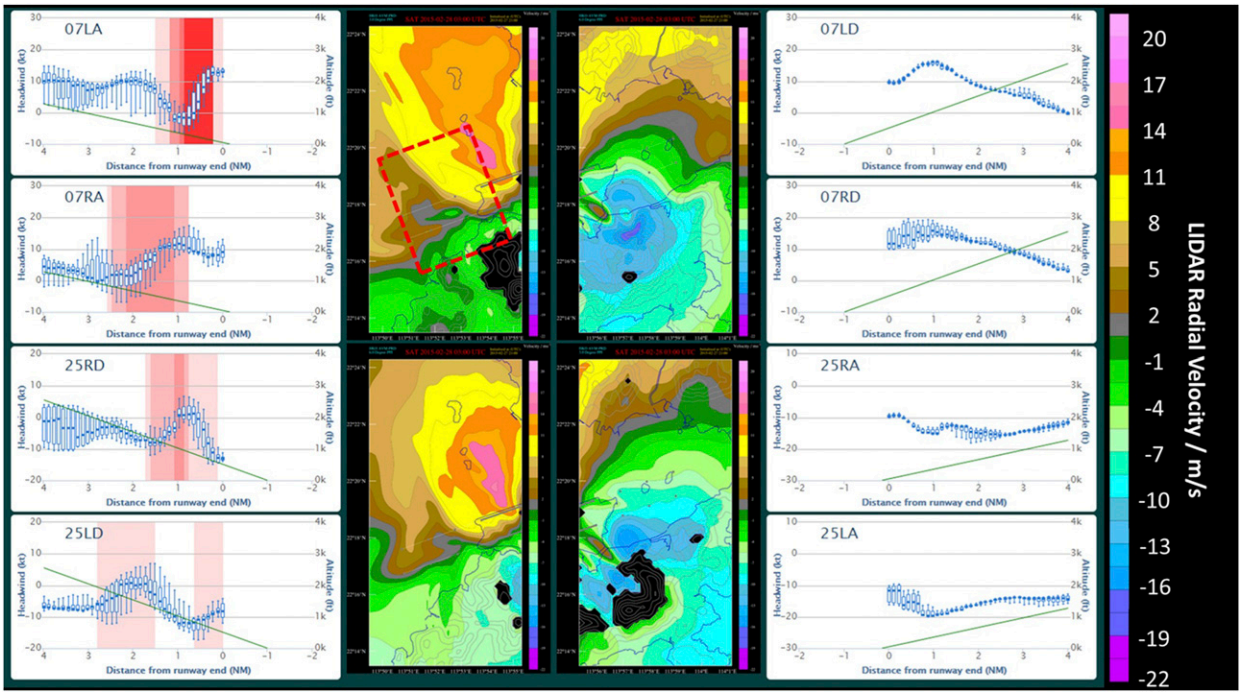

FIG. 6. As in Fig. 2, but for the case of 28 Feb 2015. This is a 5-h forecast valid at 0200 UTC and initialized at 2100 UTC on the previous day. (center) The region of wind shear–inducing wake flow downstream of Lantau Island affecting the western side of HKIA is highlighted in red. During this hour, there are 10 PIREPs at runway corridor 07LA.

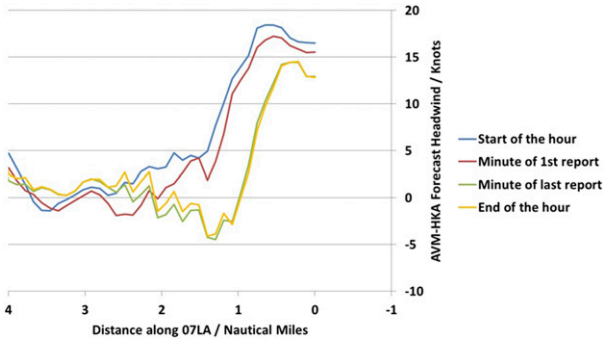

FIG. 7. Evolution of AVM-HKA forecast head wind profile during the prolonged terrain-induced wind shear episode over runway corridor 07LA as illustrated in Fig. 6. Here the x axis is reversed to reflect that the aircraft arrives from the left-hand side (from the 4 n mi position traveling eastward to the 0 n mi position, which is touchdown). The same AVM-HKA run as in Fig. 6 is used. In this case the terrain-induced wind shear feature (mainly caused by the turbulent wake of the Lantau mountains upstream of HKIA) is sustained throughout the forecast hour: since the beginning of this hour (blue line) a sharp head wind change is visible (from +5 to +18 kt) around 1 n mi; this feature sharpens slightly by the time of the first PIREP (red line); in the subsequent minutes the head wind subsided a little but the general feature of the sharp head wind change remained (green line; from −5 to +15 kt) between 0 and 1 n mi; this lasted until the end of the hour (yellow line).

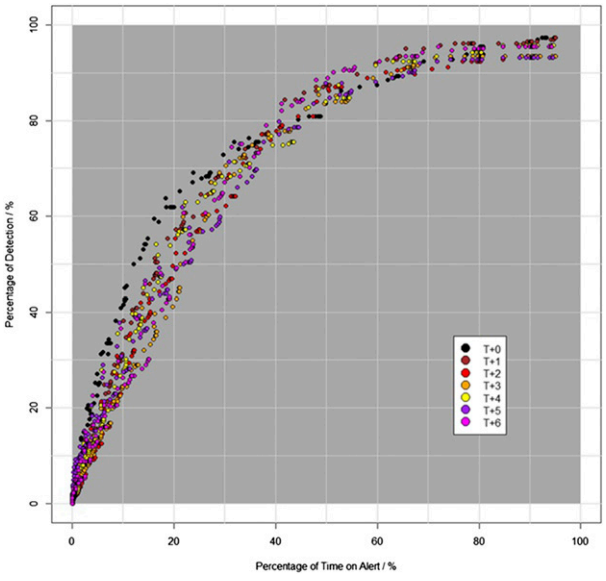

FIG. 8. ROC diagram for wind shear forecasts by AVM-HKA for runway corridor 07LA for the 1-yr period covering the whole of 2014. Different forecast lead times are marked using different colors. Each dot is a point on an ROC curve generated by varying the thresholds on ΔH_L and L to obtain binary forecasts of wind shear events using AVM-HKA forecast head wind profiles at 1-min output intervals. A "T + 0" forecast by AVM-HKA refers to a forecast head wind profile with a valid time between T + 0 and T + 59 min (i.e., the zeroth hour), a "T + 1" forecast refers to between T + 1 h and T + 1 h 59 min, etc.

NWP models (Ellrod and Knox 2010). Similar ROC behavior could be observed for NWP forecasts of CAT before the application of sophisticated ensemble and statistical postprocessing techniques (Sharman and Pearson 2017).

There does not appear to be a definitive trend in prediction skill across different forecast lead times. For example, for 07LA in 2015 (Fig. 9), the "T + 6" forecast (magenta) is the most skillful while the "T + 2" (red) and "T + 3" (orange) forecasts appear relatively least skillful. This trend is less clear cut in 2014 (Fig. 8), with the ROC curves of different lead times generally mixed together. Prediction skill also displays different behavior across runway corridors. For 25RA, the "T + 2" (red) and "T + 3" (orange) forecasts appear to show highest skill level in both 2014 and 2015 while the longer-range forecasts ("T + 4," "T + 5," and "T + 6," respectively in yellow, purple, and magenta) have relatively little skill. The "T + 0" forecasts (available only in 2014 for both runway corridors) show higher skill level over 07LA, particular for PoTA below 30%, but the "T + 0" forecasts for 25RA do not show visibly more skill than the other forecast hours. There are a number of possible, competing factors contributing to the lack of observed trend in prediction skill across lead times. One would naturally expect forecast skill to decay gradually with increasing lead time, as a simple consequence of atmospheric predictability (Lorenz 1963). On the other hand, since AVM-HKA is run on a "cold start" basis without cycling of model output from previous forecast hours, the gradual "spinup" of turbulent features during the first few hours of forecasts (Kealy et al. 2019) might contribute to an increase of skill level with lead time, given the relatively short forecast duration of the AVM system. Last, the assimilation of dense surface observations at and around HKIA (including a network of anemometers and weather buoys spaced at around 1 n mi, or 1.852 km, apart) may have some positive contributions around the time of model initialization. It may be conjectured that there are complex interplay of the above competing factors at the microscale, which would require in-depth analysis (possibly with spectral, or Fourier transform, methods) to delineate (e.g., Skamarock 2004; Mirocha et al. 2014).

Observational studies have indicated that low-level wind shear at HKIA is a phenomenon with high spatiotemporal variability (Tang et al. 2011a,b). In addition, individual wind shear events may be transient and sporadic in nature (Shun and Chan 2008). These physical characteristics can be expected to bring considerable technical challenges in the numerical prediction—as opposed to *detection*—of low-level wind shear. According to Skamarock (2004), the effective resolution (i.e., the

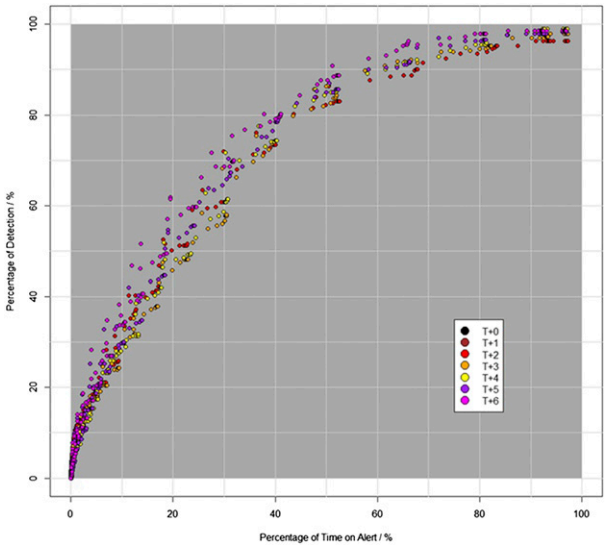

FIG. 9. As in Fig. 8, but for the 1-yr period covering the whole of 2015. Note that "$T + 0$" forecasts are not available for 2015.

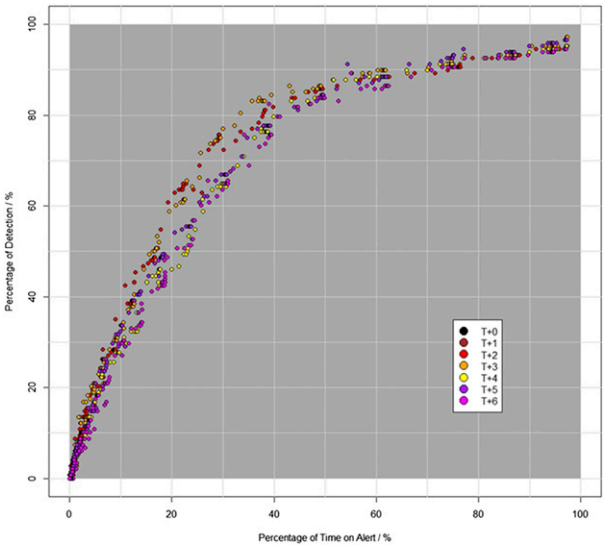

FIG. 11. As in Fig. 10, but for the 1-yr period covering the whole of 2015. Note that "$T + 0$" forecasts are not available for 2015.

wavelength of the smallest eddies in the kinetic energy spectrum effectively represented by the NWP model) of the WRF Model would be around 5–7 times the horizontal grid spacing. Here, with the 200-m nominal resolution of AVM-HKA, it could be expected that eddies on the order of 1–1.4 km may be effectively resolved. This is comparable to the length scale of certain known wind shear features at HKIA (Tang et al. 2011a; Wu and Hon 2018), which could explain in part the definitive positive skill exhibited by AVM-HKA throughout the scope of this study. On the other hand, more recent observational studies with even higher-resolution remote sensing instruments (Hon et al. 2014) have revealed other wind shear–inducing flow phenomena of even smaller spatial and temporal scales (on the order of a couple hundred meters and lasting only 1 or 2 min). These phenomena are naturally beyond the prediction capability of the existing AVM-HKA.

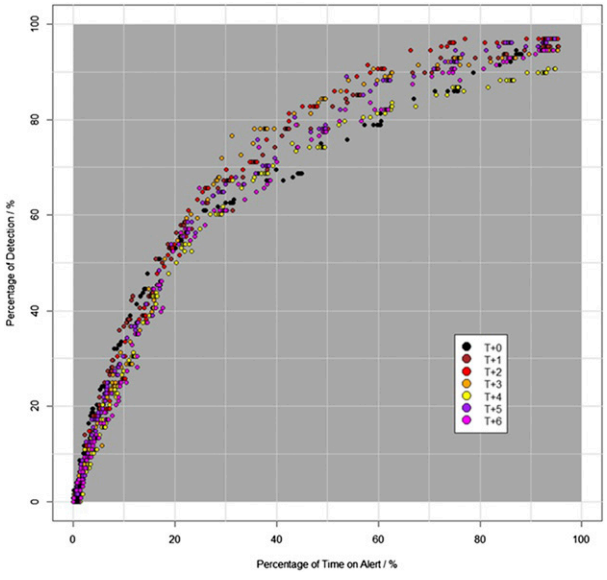

FIG. 10. As in Fig. 8, but for runway corridor 25RA.

At all times during the study we bear in mind that in reality the atmosphere is a three-dimensional fluid and the full vector wind consists of three orthogonal components. We recognize the potential theoretical limitations in leaving out the vertical wind component (and its spatial variations) in our analysis, whether in remote sensing observations or model simulations of the wind shear conditions. However, we note too from a practical point of view that, given the highly inhomogeneous environment and airflow around HKIA, it would pose considerable technical hurdles to make reliable measurements of the vertical wind component (and its gradient) along any stretch of spatial distance to the same level of accuracy as the lidar head wind profiles. Without such measurements, it would not be practical to base event predictions of the NWP model on vertical wind components in the boundary layer, which might themselves exhibit certain deficiencies (Gibbs and Fedorovich 2014; Shin and Dudhia 2016). Our current definition, and choice, of wind shear can be to an extent justified by the operational successes of those remote sensing and in situ systems that are based on the horizontal (or slanted) shear of the horizontal winds (of which head wind is a subset) at airports around the world.

The verification scheme used in the current study follows that of detection-based alerting systems that are operationally used. This scheme is rather demanding in terms of simultaneous location and timing accuracy. High-resolution NWP is known to be sensitive to phase errors (Ebert et al. 2013) due to incorrect positioning of weather systems in parent model domains. For AVM-HKA, a shift of only a few grid points in the 2-km RAPIDS-NHM boundary or initial conditions is already capable of putting a certain weather phenomenon well away from HKIA (which is only about 4 km across in length). It must be considered quite remarkable already, that positive skill is consistently obtained throughout the current study. At the time of writing, the fine-resolution winds and temperature fields of AVM-HKA are already routinely referenced by aviation weather forecasters at HKIA in their operational forecasting process. Postprocessed wind shear prediction products, such as the condensed display format in Figs. 2 and 6, could be expected to assist the forecaster in making broad, qualitative assessments covering the next few hours.

6. Conclusions

For the first time, statistical evaluation of NWP model performance in the prediction of low-level wind shear, a high-impact aviation weather phenomenon, is performed. Forecast head wind profiles, which emulate the wind components experienced by an aircraft during the takeoff or landing phase, are generated at 1-min output intervals using short-term forecasts from the 200-m-resolution AVM-HKA, which is the HKO's subkilometer-resolution WRF-based NWP suite serving the HKIA. The HKIA is situated near complex terrain and is known for its susceptibility to occurrence of various forms of low-level wind shear. Predictions of wind shear specific to each of the eight runway corridors of HKIA are generated using a threshold-based approach and compared against actual reports of wind shear by pilots landing at or taking off from HKIA using a verification scheme with the same level of spatial and temporal accuracy requirements as operational low-level wind shear alerting systems at HKIA based on remote sensing detection. A 2-yr study period from January 2014 to December 2015 is used, covering over 800 events reported over the two major arrival runway corridors of 07LA and 25RA. These wind shear events occurred under a number of different meteorological conditions including sea breeze, convection, and terrain-disrupted airflow in the vicinity of HKIA. Based on ROC analysis, positive skill is consistently observed across both runway corridors throughout the study period and across all considered forecast lead times out to $T + 6$ h ahead. This study serves to establish and document the current capability of fine-resolution NWP in predicting the phenomenon of low-level wind shear for aviation weather applications, which so far is almost exclusively alerted using high-resolution remote sensing equipment on a detection basis when done automatically.

Acknowledgments. The Hong Kong Airline Pilots Association (HKALPA) is gratefully acknowledged for the permission to use deidentified pilot reports of low-level wind shear for scientific research purposes. The author thanks the three anonymous reviewers and Dr. Katherine Klink for many useful comments and suggestions.

REFERENCES

Boutle, I. A., A. Finnenkoetter, A. P. Lock, and H. Wells, 2016: The London Model: Forecasting fog at 333 m resolution. *Quart. J. Roy. Meteor. Soc.*, **142**, 360–371, https://doi.org/10.1002/qj.2656.

Carruthers, D., A. Ellies, J. Hunt, and P. W. Chan, 2014: Modelling of wind shear downwind of mountain ridges at Hong Kong International Airport. *Meteor. Appl.*, **21**, 94–104, https://doi.org/10.1002/met.1350.

Chan, P. W., C. M. Shun, and M. L. Kuo, 2010: Latest developments of windshear alerting services at the Hong Kong International Airport. *14th Conf. on Aviation, Range, and Aerospace Meteorology*, Atlanta, GA, Amer. Meteor. Soc., 10.4, https://ams.confex.com/ams/pdfpapers/157792.pdf.

——, and K. K. Hon, 2016a: Observation and numerical simulation of terrain-induced windshear at the Hong Kong International Airport in a planetary boundary layer without temperature inversions. *Adv. Meteor.*, **2016**, 1454513, https://doi.org/10.1155/2016/1454513.

——, and ——, 2016b: Performance of super high resolution numerical weather prediction model in forecasting terrain-disrupted airflow at the Hong Kong International Airport: Case studies. *Meteor. Appl.*, **23**, 101–114, https://doi.org/10.1002/met.1534.

——, ——, and D. K. Shin, 2011: Combined use of headwind ramps and gradients based on lidar data in the alerting of low-level windshear/turbulence. *Meteor. Z.*, **20**, 661–670, https://doi.org/10.1127/0941-2948/2011/0242.

——, ——, and Q. S. Li, 2020: A more comprehensive study of terrain-disrupted airflow at the Hong Kong International Airport—Observations and numerical simulations. *Weather*, https://doi.org/10.1002/wea.3593, in press.

Cheung, J. O. P., P. W. Chan, and D. Y. C. Leung, 2011: Large-eddy simulation of the wind flow across a terminal building on the airfield. *Int. J. Earth Sci. Eng.*, **4**, 486–489.

Clark, T. L., T. Keller, J. Coen, P. Neilley, H. Hsu, and W. D. Hall, 1997: Terrain-induced turbulence over Lantau Island: 7 June 1994 Tropical Storm Russ case study. *J. Atmos. Sci.*, **54**, 1795–1814, https://doi.org/10.1175/1520-0469(1997)054<1795:TITOLI>2.0.CO;2.

Ebert, E., and Coauthors, 2013: Progress and challenges in forecast verification. *Meteor. Appl.*, **20**, 130–139, https://doi.org/10.1002/met.1392.

Ellrod, G. P., and D. I. Knapp, 1992: An objective clear-air turbulence forecasting technique: Verification and operational

use. *Wea. Forecasting*, **7**, 150–165, https://doi.org/10.1175/1520-0434(1992)007<0150:AOCATF>2.0.CO;2.

——, and J. A. Knox, 2010: Improvements to an operational clear-air turbulence diagnostic index by addition of a divergence trend term. *Wea. Forecasting*, **25**, 789–798, https://doi.org/10.1175/2009WAF2222290.1.

Fujita, T. T., 1978: Manual of downburst identification for project NIMROD. University of Chicago Dept. of the Geophysical Sciences Satellite and Mesometeorology Research Project Research Paper 156, 104 pp., https://ntrs.nasa.gov/archive/nasa/casi.ntrs.nasa.gov/19780022828.pdf.

Gibbs, J. A., and E. Fedorovich, 2014: Comparison of convective boundary layer velocity spectra retrieved from large-eddy-simulation and weather research and forecasting model data. *J. Appl. Meteor. Climatol.*, **53**, 377–394, https://doi.org/10.1175/JAMC-D-13-033.1.

Hagelin, S., L. Auger, P. Brovelli, and O. Dupont, 2014: Nowcasting with the AROME model: First results from the high-resolution AROME airport. *Wea. Forecasting*, **29**, 773–787, https://doi.org/10.1175/WAF-D-13-00083.1.

Hall, F., W. Neff, and T. Frazier, 1976: Wind shear observations in thunderstorm density currents. *Nature*, **264**, 408–411, https://doi.org/10.1038/264408a0.

Heinze, R., and Coauthors, 2017: Large-eddy simulations over Germany using ICON: A comprehensive evaluation. *Quart. J. Roy. Meteor. Soc.*, **143**, 69–100, https://doi.org/10.1002/qj.2947.

Hon, K. K., 2018: Simulated satellite imagery at sub-kilometre resolution by the Hong Kong observatory. *Weather*, **73**, 139–144, https://doi.org/10.1002/wea.3100.

——, and P. W. Chan, 2014a: Terrain-induced turbulence intensity during tropical cyclone passage as determined from airborne, ground-based, and remote sensing sources. *J. Atmos. Oceanic Technol.*, **31**, 2373–2391, https://doi.org/10.1175/JTECH-D-14-00006.1.

——, and ——, 2014b: Application of lidar-derived eddy dissipation rate profiles in low-level wind shear and turbulence alerts at Hong Kong International Airport. *Meteor. Appl.*, **21**, 74–85, https://doi.org/10.1002/met.1430.

——, and ——, 2017: Frequent-output sub-kilometric NWP models supporting enhanced runway throughput and performance-based navigation. *Aeronautical Meteorology Scientific Conf.*, Toulouse, France, WMO, https://www.wmo.int/aemp/sites/default/files/Presentation_Hon_Session1_AeroMetSci-2017.pdf.

——, ——, Y. Y. Chiu, and W. Tang, 2014: Application of short-range lidar in early alerting for low-level windshear and turbulence at Hong Kong International Airport. *Adv. Meteor.*, **2014**, 162748, https://doi.org/10.1155/2014/162748.

——, S. M. Tse, P. W. Chan, and Q. S. Li, 2019: Observation and real-time simulation of a tornado event in Hong Kong on 29 August 2018. *Adv. Meteor.*, **2019**, 8571430, https://doi.org/10.1155/2019/8571430.

Hong Kong Observatory, 2010: *Windshear and Turbulence in Hong Kong–Information for Pilots*. 3rd ed. Hong Kong Observatory, 24 pp, https://www.hko.gov.hk/en/aviat/articles/files/WS-turb-booklet-eng-3rd.pdf.

Iacono, M. J., J. S. Delamere, E. J. Mlawer, M. W. Shephard, S. A. Clough, and W. D. Collins, 2008: Radiative forcing by long-lived greenhouse gases: Calculations with the AER radiative transfer models. *J. Geophys. Res.*, **113**, D13103, https://doi.org/10.1029/2008JD009944.

ICAO, 2005: *Manual on Low-Level Wind Shear and Turbulence*. 1st ed. International Civil Aviation Organization, 213 pp.

——, 2007: *Meteorological Service for International Air Navigation: Annex 3 to the Convention on International Civil Aviation*. 16th ed. International Civil Aviation Organization, 187 pp.

Janjić, Z. I., 2001: Nonsingular implementation of the Mellor-Yamada level 2.5 scheme in the NCEP Meso Model. NCEP Office Note 437, 61 pp.

Jones, J. G., and A. Haynes, 1984: A peakspotter program applied to the analysis of increments in turbulence velocity. Royal Aircraft Establishment Tech. Rep. 84071, 69 pp.

Kealy, J. C., G. A. Efstathiou, and R. J. Beare, 2019: The onset of resolved boundary-layer turbulence at grey-zone resolutions. *Bound.-Layer Meteor.*, **171**, 31–52, https://doi.org/10.1007/s10546-018-0420-0.

Lau, S. Y., 2000: Windshear and turbulence detection and warning at the Hong Kong International Airport. *Proc. Working Group on Training, The Environment and New Developments (TREND), Commission for Aeronautical Meteorology*, Hong Kong, China, World Meteorological Organization, https://www.hko.gov.hk/en/publica/reprint/files/r371.pdf.

Lee, Y. F., and P. W. Chan, 2014: Lidar-based F-factor for wind shear alerting: Different smoothing algorithms and application to departing flights. *Meteor. Appl.*, **21**, 86–93, https://doi.org/10.1002/met.1434.

Leung, M. Y. T., W. Zhou, C. M. Shun, and P. W. Chan, 2018: Large-scale circulation control of the occurrence of low-level turbulence at Hong Kong International Airport. *Adv. Atmos. Sci.*, **35**, 435–444, https://doi.org/10.1007/s00376-017-7118-y.

Li, L., P. W. Chan, L. Zhang, and F. Hu, 2013: Numerical simulation of a Lee wave case over three-dimensional mountainous terrain under strong wind condition. *Adv. Meteor.*, **2013**, 304321, https://doi.org/10.1155/2013/304321.

Lim, K.-S. S., and S.-Y. Hong, 2010: Development of an effective double–moment cloud microphysics scheme with prognostic cloud condensation nuclei (CCN) for weather and climate models. *Mon. Wea. Rev.*, **138**, 1587–1612, https://doi.org/10.1175/2009MWR2968.1.

Lorenz, E. N., 1963: Deterministic nonperiodic flow. *J. Atmos. Sci.*, **20**, 130–141, https://doi.org/10.1175/1520-0469(1963)020<0130:DNF>2.0.CO;2.

Matayoshi, N., T. Ijima, K. Yamamoto, and E. Fujita, 2016: Development of Airport Low-level Wind Information (ALWIN). *16th AIAA Aviation Technology, Integration, and Operations Conf.*, Washington, DC, American Institute of Aeronautics and Astronautics, AIAA 2016-4362, https://doi.org/10.2514/6.2016-4362.

Mellor, G. L., and T. Yamada, 1982: Development of a turbulence closure model for geophysical fluid problems. *Rev. Geophys.*, **20**, 851–875, https://doi.org/10.1029/RG020i004p00851.

Mirocha, J., B. Kosović, and G. Kirkil, 2014: Resolved turbulence characteristics in large-eddy simulations nested within mesoscale simulations using the Weather Research and Forecasting Model. *Mon. Wea. Rev.*, **142**, 806–831, https://doi.org/10.1175/MWR-D-13-00064.1.

Niu, G. Y., and Coauthors, 2011: The community Noah land surface model with multiparameterization options (Noah–MP): 1. Model description and evaluation with local–scale measurements. *J. Geophys. Res.*, **116**, D12109, https://doi.org/10.1029/2010JD015139.

Proctor, F. H., D. A. Hinton, and R. L. Bowles, 2000: A windshear hazard index. Preprints, *Ninth Conf. on Aviation, Range, and Aerospace Meteorology*, Orlando, FL, Amer. Meteor. Soc., 7.7, https://ams.confex.com/ams/Sept2000/techprogram/paper_16347.htm.

Robinson, D. C., D. Collins, J. Brett, J. Klewicki, and P. Murray, 2017: Airport building development: Towards a framework for managing building-induced wind shear and turbulence risks. *J. Airport Manage.*, **11**, 369–385.

Sharman, R. D., and J. M. Pearson, 2017: Prediction of energy dissipation rates for aviation turbulence. Part I: Forecasting nonconvective turbulence. *J. Appl. Meteor. Climatol.*, **56**, 317–337, https://doi.org/10.1175/JAMC-D-16-0205.1.

Shin, H. H., and J. Dudhia, 2016: Evaluation of PBL parameterizations in WRF at subkilometer grid spacings: Turbulence statistics in the dry convective boundary layer. *Mon. Wea. Rev.*, **144**, 1161–1177, https://doi.org/10.1175/MWR-D-15-0208.1.

Shun, C. M., 2004: Wind shear and turbulence alerting at Hong Kong International Airport. *WMO Bull.*, **53**, 316–320.

——, and S. Y. Lau, 2000: Terminal Doppler Weather Radar (TDWR) observation of atmospheric flow over complex terrain during tropical cyclone passages. *Proc. SPIE*, **4152**, 42–53, https://doi.org/10.1117/12.410622.

——, and P. W. Chan, 2008: Applications of an infrared Doppler lidar in detection of wind shear. *J. Atmos. Oceanic Technol.*, **25**, 637–655, https://doi.org/10.1175/2007JTECHA1057.1.

Skamarock, W. C., 2004: Evaluating mesoscale NWP models using kinetic energy spectra. *Mon. Wea. Rev.*, **132**, 3019–3032, https://doi.org/10.1175/MWR2830.1.

——, and J. B. Klemp, 2008: A time-split nonhydrostatic atmospheric model for weather research and forecasting applications. *J. Comput. Phys.*, **227**, 3465–3485, https://doi.org/10.1016/j.jcp.2007.01.037.

Szeto, K. C., and P. W. Chan, 2006: High resolution numerical modelling of windshear episodes at the Hong Kong International Airport. *12th Conf. on Aviation, Range, and Aerospace Meteorology*, Atlanta, GA, Amer. Meteor. Soc., P5.8, https://ams.confex.com/ams/pdfpapers/100319.pdf.

Talbot, C., E. Bou-Zeid, and J. Smith, 2012: Nested mesoscale large-eddy simulations with WRF: Performance in real test cases. *J. Hydrometeor.*, **13**, 1421–1441, https://doi.org/10.1175/JHM-D-11-048.1.

Tang, W., P. W. Chan, and G. Haller, 2011a: Lagrangian coherent structure analysis of terminal winds detected by lidar. Part I: Turbulence structures. *J. Appl. Meteor. Climatol.*, **50**, 325–338, https://doi.org/10.1175/2010JAMC2508.1.

——, ——, and ——, 2011b: Lagrangian coherent structure analysis of terminal winds detected by lidar. Part II: Structure evolution and comparison with flight data. *J. Appl. Meteor. Climatol.*, **50**, 2167–2183, https://doi.org/10.1175/2011JAMC2689.1.

Wilks, D. S., 2006: *Statistical Methods in the Atmospheric Sciences*. 2nd ed. Academic Press, 627 pp.

Wilson, J. W., and R. M. Wakimoto, 2001: The discovery of the downburst: T. T. Fujita's contribution. *Bull. Amer. Meteor. Soc.*, **82**, 49–62, https://doi.org/10.1175/1520-0477(2001)082<0049:TDOTDT>2.3.CO;2.

Wong, W. K., 2010: Development of operational rapid update nonhydrostatic NWP and data assimilation systems in the Hong Kong Observatory. *Third Int. Workshop on Prevention and Mitigation of Meteorological Disasters in Southeast Asia*, Beppu, Japan, https://www.hko.gov.hk/tc/publica/reprint/files/r882.pdf.

Wu, T. C., and K. K. Hon, 2018: Application of spectral decomposition of lidar-based headwind profiles in windshear detection at the Hong Kong International Airport. *Meteor. Z.*, **27**, 33–42, https://doi.org/10.1127/metz/2017/0858.

Zhang, H., Z. Pu, and X. Zhang, 2013: Examination of errors in near-surface temperature and wind from WRF numerical simulations in regions of complex terrain. *Wea. Forecasting*, **28**, 893–914, https://doi.org/10.1175/WAF-D-12-00109.1.